



Constructing desired interfacial energy band alignment of Z-scheme $\text{TiO}_2\text{-Pd-Cu}_2\text{O}$ hybrid by controlling the contact facet for improved photocatalytic performance



Fei Ye^a, Yan Su^b, Xie Quan^{a,*}, Shuo Chen^a, Hongtao Yu^a, Houfen Li^c

^a Key Laboratory of Industrial Ecology and Environmental Engineering (Ministry of Education, China), School of Environmental Science and Technology, Dalian University of Technology, Dalian, 116024, China

^b Key Laboratory of Materials Modification by Laser, Ion and Electron Beams (Ministry of Education), School of Physics, Dalian University of Technology, Dalian, 116024, China

^c College of Environmental Science and Engineering, Taiyuan University of Technology, Taiyuan, 030024, China

ARTICLE INFO

Keywords:

Energy band alignment
Work function
Crystal facet
Z-scheme
Photocatalysis

ABSTRACT

Interfacial energy band alignment determines the charges transfer path at the interface of semiconductor-based Z-scheme photocatalytic system. Herein, an elaborately designed $\text{TiO}_2\text{-Pd-Cu}_2\text{O}$ Z-scheme hybrid, with desired energy band alignment for simultaneously facilitating electrons transfer from TiO_2 to Pd and holes transfer from Cu_2O to Pd, is achieved by controlling the $\text{TiO}_2\{001\}$ facet, $\text{Cu}_2\text{O}\{100\}$ facet and Pd as Photosystem II (PS II), Photosystem I (PS I) and electron mediator, respectively. The $\text{TiO}_2\{001\}\text{-Pd-Cu}_2\text{O}\{100\}$ hybrid exhibits 1.37–3.12 times higher photocurrent density and 1.22–2.06 folds higher phenol degradation efficiency than other three hybrids with $\text{TiO}_2\{101\}$ facet or $\text{Cu}_2\text{O}\{111\}$ facet contacted with Pd at the interface. Density Function Theory (DFT) calculations reveal that the work functions are in order of $\text{TiO}_2\{001\} < \text{Pd} < \text{Cu}_2\text{O}\{100\}$, which facilitates both electrons transfer from $\text{TiO}_2\{001\}$ facet to Pd and holes transfer from $\text{Cu}_2\text{O}\{100\}$ facet to Pd, hence remains the high-energy electrons on $\text{Cu}_2\text{O}\{100\}$ facet and high-energy holes on $\text{TiO}_2\{001\}$ facet for efficient degradation of organic pollutants. This work gives an insight on rational construction of Z-scheme photocatalytic system depending on the energy band alignment of contact facets.

1. Introduction

The artificial Z-scheme system is an effective construction to improve the photocatalytic performance of photocatalysts, which generally contains photosystem I (PS I), photosystem II (PS II) and an electron mediator [1–5]. During light irradiation, electrons generated on PS II transfer through electron mediator to recombine with holes generated on PS I at the interface, and the corresponding electrons with higher reductive ability on PS I and holes with higher oxidative ability on PS II are thereby retained [3,6,7]. As energetic separation of charge-carrier between PS I and PS II is a key factor for achieving efficient Z-scheme system, various efforts [8–10] have been devoted to improve the interfacial charge carriers separation. For example, our previous work provides scientific basis for construction of Z-scheme system with suitable interfacial energy band bending, in which the relative position of the Fermi level of electron mediator (Cu) located between the Fermi levels of PS I (C_3N_4) and PS II (WO_3) was proposed to promote interfacial charge carriers transportation through a Z-scheme mechanism

[11]. On the other hand, according to the property of facet induced charge separation in well-faceted crystal photocatalyst, we selectively deposited Au nanoparticles on electrons accumulated $\{010\}$ facet of BiVO_4 , which facilitated the interfacial charge carrier separation of $\text{BiVO}_4\text{-Au@CdS}$ Z-scheme system [12]. Based on previous studies, the role of facet-induced energy band differences between PS I (or PS II) and electron mediator on interfacial charge transfer would be a key factor for achieving an efficient Z-scheme system. However, to the best of our knowledge, essentially limited study has concerned the facet effects on the electrons-holes transfer at Z-scheme system interfaces.

As a typical example of a PS I photocatalyst, Cu_2O has different energy band structures for its various surface, which endows it with various charge separation abilities [13–15]. Wang and co-workers proved that the $\{100\}$ facet of Cu_2O nanocubes, with a higher work function (7.25 eV) than Pd, is favorable for the migration of holes from the Cu_2O surface to Pd through forming a Schottky junction, while Cu_2O octahedra with $\{111\}$ facet exposed has a lower work function (4.83 eV) than Pd show opposite effect [16,17]. Meanwhile, TiO_2 as a

* Corresponding author.

E-mail address: quanxie@dlut.edu.cn (X. Quan).

commonly used PS II photocatalyst has also been observed with higher electrons donating ability on the {001} facet than its {101} facet owing to the fact that lower work function of {001} facet (5.78 eV) than {101} facet (6.76 eV) can decrease the charge transfer barrier between semiconductor and metal [18]. Based on these analyses, one would assume that the optimal photocatalytic performance could be achieved if contacting the {100} facet of Cu₂O and the {001} facet of TiO₂ with Pd in a Z-scheme system. As the favorable energy band structure for holes transfer in Cu₂O-Pd and electrons transfer in TiO₂-Pd heterojunction also facilitates efficient charge transfer at the interface of Z-scheme system TiO₂-Pd-Cu₂O.

Herein, taking TiO₂, Pd and Cu₂O as PS II, electron mediator and PS I, respectively. We designed four facet based Z-scheme TiO₂-Pd-Cu₂O hybrids through two-step reactions to selectively grow Pd nanocubes, and Cu₂O nanostructures with {100} or {111} facet exposed on the {001} facet and {101} facet of TiO₂ nanocrystals, respectively, to uncover the facet effects on electron-hole transfer at the interface. Both photocurrent and photoluminescence analysis reveal that the Z-scheme TiO₂{001}-Pd-Cu₂O{100} interface composed of TiO₂{001} and Cu₂O {100} contacted with Pd nanocubes displays the superior charge carriers separation capacity, while TiO₂{101}-Pd-Cu₂O{111} exhibits the inferior property. Correspondingly, the former hybrid promises the optimal photocatalytic performance among all the four TiO₂-Pd-Cu₂O Z-scheme hybrids. Density Function Theory (DFT) simulations further verified that the interfacial band energy alignment of TiO₂{001}-Pd-Cu₂O{100} is favorable for interfacial charge separation, and preserved more holes and electrons with high redox ability on TiO₂{001} and Cu₂O{100}, respectively. This work opened up a new direction to the design and synthesis of facet based Z-scheme photocatalysts with improved photocatalytic performance.

2. Experiment section

2.1. Preparation of catalysts

2.1.1. Synthesis of Z-scheme TiO₂-Pd-Cu₂O hybrids

The Z-scheme TiO₂-Pd-Cu₂O hybrids were synthesized through a three-step process.

Step 1: Synthesis of TiO₂ nanosheets and octahedra

TiO₂ nanosheets with mainly {001} facet exposed (donated as T001) were prepared through a hydrothermal process according to previously reported procedures [19]. In brief, 10 mL of Ti(OBu)₄ and 4 mL HF solution were mixed together in a dried 50 mL Teflon-lined autoclave under stirring. Then 10 mL anhydrous ethanol was dropwise added into the above liquid. After that, the reaction was carried out at 200 °C for 24 h. TiO₂ octahedra exposing its {101} facet (donated as T101) were synthesized through a two-step hydrothermal procedure according to previous reports [20]. Firstly, P25 (1 g) was reacted hydrothermally with KOH solution (70 mL, 10 M) in a 100 mL Teflon-lined autoclave at 110 °C for 20 h. The resulting precipitate (potassium titanate) was collected by filtration, and then washed and dried. Secondly, the prepared potassium titanate (100 mg) was stirred in deionized water (30 mL) and heated in a 100 mL Teflon-lined autoclave at 170 °C for 24 h.

Step 2: Synthesis of TiO₂-Pd precursor

In a typical synthesis of TiO₂{001}-Pd or TiO₂{101}-Pd precursor (donated as T001-P or T101-P) [21], 80 μL K₂PdCl₄ (1 g/50 mL) solution, 45.5 mg CTAB and 5 mg TiO₂ powers (T001 or T101) were first mixed in 10 mL deionized water under stirring and preheated at 100 °C for 10 min. Then 80 μL ascorbic acid solution (0.1 M) was added and the mixed solution was allowed to react at 100 °C for another 5 min. The product was obtained through centrifugation, and then washed and dried. The T001-P and T101-P powders were redispersed in water for subsequent use.

Step 3: Synthesis of TiO₂-Pd-Cu₂O Z-scheme photocatalysts

In a typical synthesis process of TiO₂{001}-Pd-Cu₂O{100} or

TiO₂{101}-Pd-Cu₂O{100} hybrids (donated as T001-P-C100 or T101-P-C100), 8.8 mL deionized water was first introduced into a 20 mL sample vial, subsequently 0.1 mL CuSO₄ solution (0.1 M) and 1 mL aqueous dispersion of as-synthesized T001-P (or T101-P) were added in above deionized water under stirring. Followed by introduction of 600 μL NaOH solution (1 M) the resulting solution turned light blue, indicating the formation of Cu(OH)₂ precipitate. Upon addition of 500 μL ascorbic acid solution (0.2 M), the solution turned bright yellow immediately. The solution was stirred for 10 min and then was kept in a 35 °C water bath to yield the products [22]. To synthesize TiO₂{001}-Pd-Cu₂O {111} or TiO₂{101}-Pd-Cu₂O{111} (donated as T001-P-C111 or T101-P-C111), 7.0 mL deionized water was first introduced into a 20 mL sample vial, subsequently 100 μL Cu(OAC) solution (0.1 M) and 1 mL aqueous dispersion of as-synthesized T001-P (or T101-P) were added under stirring. After introduction of 100 μL NaOH solution (0.1 M) the resulting solution turned light blue, indicating the formation of Cu(OH)₂ precipitate. Followed by addition of 2.8 mL N₂H₄ solution (0.2 M), the solution turned bright yellow immediately. The solution was stirred for 30 min and then kept in a 50 °C water bath to yield the products [23]. To collect the products, the solution was centrifuged, and then washed and dried. To convenient for comparing the photocatalytic performance among C100 based catalysts, the labels of C100-P-T001 and C100-P-T101 will in place of T001-P-C100 and T101-P-C100, respectively. So will C111 based catalysts.

2.1.2. Synthesis of bare Cu₂O nanocubes, octahedra and Pd-Cu₂O core-shell structure

Cu₂O nanocubes (donated as C100) and octahedra (donated as C111) were synthesized under the same experimental conditions as the TiO₂-Pd-Cu₂O except without the addition of TiO₂-Pd precursors. The Pd-Cu₂O core–shell structure (donated as P-C100 or P-C111) was prepared under the same experimental conditions as the TiO₂-Pd-Cu₂O except for the use of bare Pd nanocubes instead of TiO₂-Pd as precursors. Bare Pd nanocubes were synthesized under the same experimental conditions as the TiO₂-Pd nanocubes except without the addition of TiO₂ precursors.

2.2. Characterization

The morphologies and microstructures of the samples were observed through an S-4800 field emission scanning electron microscope (SEM, Hitachi) and a G² F30 transmission electron microscope (TEM, FEI-Tecnai), respectively. The crystal structures were investigated using an X-ray diffractometer (XRD, Rigaku SmartLab9) and the X-ray photoelectron spectra (XPS) were collected on an ESCALAB 250XI X-ray photoelectron spectrometer with a Al $\text{K}\alpha$ source (1486.6 eV). UV-vis diffuse reflectance spectra (DRS) of the powders were measured on a Shimadzu UV-2450 spectrophotometer in spectral region of 300–800 nm. Photoluminescence (PL) spectra of the samples were recorded on a Hitachi F-4500 spectrometer. The superoxide radicals (O_2^-) and hydroxyl radicals ($\cdot\text{OH}$) were detected on an electron spin resonance (ESR) spectrometer (A200, Bruker) in methanol solution and aqueous solution, respectively, with 5,5-dimethyl 1-l-pyrroline-n-oxide (DMPO, 50 mM) as a spin trap to stabilize the radicals.

2.3. Photoelectrochemical measurements

The photocurrents were measured on a CHI 660D electrochemical workstation (Shanghai Chenhua, China). A three-electrode setup was used in 0.1 M Na₂SO₄ electrolyte, with samples coated on conductive glass as the working electrode, a Pt sheet as counter electrode and saturated calomel electrode (SCE) as reference electrode, respectively. The photocurrent response of working electrode was operated at a bias potential of 0 V A 500 W xenon arc lamp (Zolix LSP-X500, Beijing Zhuolihanguang) was used as a solar light source, and the incident light intensity was 100 mW/cm². The electrochemical impedance

spectroscopy (EIS) was performed in the 10^{-1} to 10^6 Hz frequency range with an AC voltage amplitude of 10 mV at an applied potential of 0 V versus SCE. The transient open-circuit voltage decay (OCVD) measurements were taken for 250 s in all and the light on and off were controlled at 50 and 150 s, respectively.

2.4. Photocatalytic reactions

The photocatalytic performance of samples were evaluated in degradation of phenol. A 500 W xenon arc lamp was used as a solar light source. Before irradiation, 5 mg photocatalyst was added to a 20 mL phenol solution (10 mg/L) under stirring in the dark for 30 min to reach adsorption-desorption equilibrium. The phenol concentration was determined by high-performance liquid chromatography (Waters 2695, USA) equipped with a photodiode array detector (Waters 2996). The total organic carbon (TOC) removal was measured through a TOC analyzer (multi N/C 2100S, Analytikjena, Germany).

2.5. Calculation details

All first-principles calculations were carried out using the Vienna Ab initio Simulation Package (VASP) based on spin-polarized density functional theory (DFT) with a plane-wave basis set [24]. In order to treat the exchange-correlation interaction of electrons, the Perdew-Burke-Ernzerhof (PBE) functional [25] within the generalized gradient approximation (GGA) was chosen. The electron-ion interactions were described by the projector augmented wave (PAW) potentials [26]. An energy cutoff of 400 eV was used for the plane-wave expansion of the electronic wave function. The force and energy convergence criterion was set to 0.01 eV/Å and 10^{-4} eV, respectively. We used the Γ -centered k grids for Brillouin zone (BZ) integrations, with a uniform spacing of $2\pi \times 0.03/\text{\AA}$. Different interface structures were employed to model the hybrid configurations. For TiO_2 , we selected Ti-saturated surface for T001-P and T101-P hybrids. For Cu_2O , Cu-saturated surface was selected for constructing C100-P and C111-P hybrids.

3. Results and discussions

3.1. Structure and composition of ternary $\text{TiO}_2\text{-Pd-Cu}_2\text{O}$ hybrids

The ternary Z-scheme $\text{TiO}_2\text{-Pd-Cu}_2\text{O}$ photocatalysts were prepared in three steps as illustrated in **Scheme 1**. In the first step, TiO_2 nanocrystals, with {001} facet or {101} facet exposed, were selected as PS II, due to the existence of facet-dependent energy band structures and photocatalytic performance discrepancy between T001 and T101 [20,27,28]. Here, both T001 and T101 were prepared through hydrothermal methods, and their morphologies were observed through a scanning electron microscope. As shown in Figure S1a, b, T001 is composed of nanosheets with mainly {001} facet exposed, while T101 displays octahedral profile with {101} facet exposed. The average sizes of T001 (edge lengths) and T101 (opposite tip distance) are approximately 191 nm and 91 nm, respectively. The X-ray diffraction (XRD) patterns in Figure S2a reveal that two kinds of TiO_2 are both anatase, with obvious peaks at 25.3° and 37.8° accordance with its {101} and {004} facet (PDF# 21–1271). Moreover, the patterns of T001 show a broad {004} peak as well as a narrow {200} peak, indicating that the crystal growth was limited mainly to the {001} axis [29,30], both the XRD patterns of T001 and T101 reveal their good crystallinity.

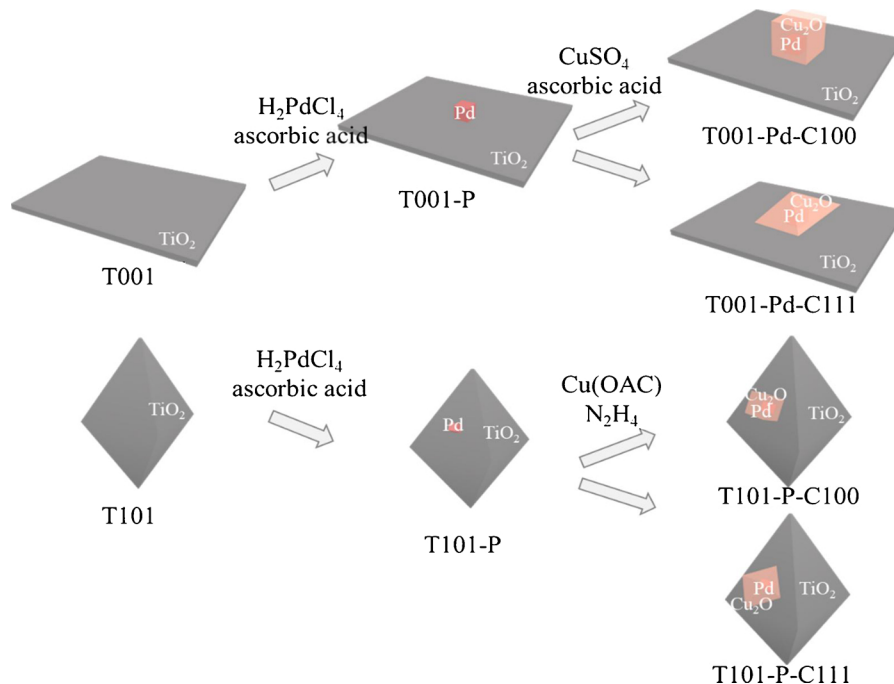
In the second step, Pd nanocubes were chosen as the mediator in the ternary Z-scheme system owing to its suitable work function position (discuss later). As shown in the SEM image (Figure S1c), the as-prepared Pd nanocrystals are in cubic profile and the edge length of them is about 17 nm. The in-situ growth of Pd nanocubes on the surface of T001 and T101 was conducted by using the same method as Pd synthesis except for the addition of TiO_2 precursors (**Scheme 1**). In comparison with the XRD patterns of T001 and T101 (Figure S2a), the additional

peaks at 40.1°, 46.7° and 68.1° were observed in the patterns of T001-P and T101-P, corresponding to fcc Pd (PDF# 65–6174) which ensures the face-to-face contact between Pd nanocrystals and TiO_2 precursors.

Thirdly, Cu_2O nanocubes (C100) with uniform edge length about 64 nm and Cu_2O octahedra (C111) with opposite tip distance about 109 nm were synthesized (Figure S1d, e), respectively, and they were respectively selected as PS I to construct ternary hybrids with T001-Pd and T101-Pd precursors (**Scheme 1**). Four facet-dependent Z-scheme photocatalysts (T001-P-C100, T001-P-C111, T101-P-C100 and T101-P-C111) were obtained through introducing T001-P and T101-P precursors during the synthesis process of Cu_2O nanocrystals (C100 and C111). According to the XRD patterns (**Fig. 1**), the crystal phase and crystallinity of Cu_2O in the ternary $\text{TiO}_2\text{-Pd-Cu}_2\text{O}$ hybrids did not change as compared with those of single crystal C100 or C111 (Figure S2b). Moreover, the diffraction peaks at 37.0° and 42.6° corresponding to (111) and (200) planes of Cu_2O were detected in all XRD patterns of the four samples, which indicating the successful introduction of Cu_2O into the systems.

The microstructures of as-prepared $\text{TiO}_2\text{-Pd-Cu}_2\text{O}$ hybrids were characterized by TEM. Before taking T001-P-C100 as an example, the microstructure of T001-P precursor was investigated. From the TEM images (**Fig. 2a, b**), it can be observed that Pd nanocrystals with cubic profile are uniformly distributed on the {001} facet of TiO_2 nanosheets and formed a T001-P hybrid structure. The HRTEM image (**Fig. 2c**) further confirmed that Pd is a monocrystal enclosed by its {100} facet with lattice spacing about 0.19 nm, thus forming a T001-P100 interface with T001. Subsequently, T001-P-C100 hybrid structure was characterized by TEM analysis. As shown in **Fig. 2d, e**, the C100 shells were selectively coated on Pd nanocubes instead of directly grown on T001 during the synthesis process, which can be ascribed to the existence of strong Pd-O interaction [14,31], facilitated the approach of Cu^{2+} towards the surface of Pd and thus contributed to subsequent Cu_2O synthesis. The HRTEM image indicates C100 is also a single crystal structure with {100} facet exposed, thus forming a ternary T001-P-C100 interfaces. The single-crystal structure of Pd and Cu_2O ensure efficient charge transfer in each component, while face-to-face contact between T001 and P100, P100 and C100 benefit interfacial charge transfer. Moreover, The P-C100 core-shell structures were also distributed on T101 nanocrystals and formed a T101-P-C100 stack structures (Figure S3a), further confirming the good selectivity of C100 towards coating on Pd nanocubes. In the meantime, the Cu_2O shells in T001-P-C111 and T101-P-C111 are in octahedral profile with lattice fringes about 0.24 nm corresponding to (111) planes of Cu_2O (Figure S3b, c). The HRTEM image shows two distinct sets of lattice fringes at the interface of core and shell regions, and a larger d-value mismatch between the {111} facet of Cu_2O and the {100} facet of Pd is speculated to account for hampering the charge transfer at the C111-P interfaces. These results along with aforementioned SEM and XRD analysis confirmed that four ternary interfaces were successfully synthesized through the three-step process.

The surface atomic composition and the chemical state of the ternary Z-scheme photocatalyst were further investigated by XPS analysis with T001-P-C100 as a typical example. **Fig. 3a** presents the XPS survey spectrum for T001-P-C100, from which all peaks corresponding to elements Ti, O, Pd and Cu were observed, confirming no impurity was introduced during the synthesis progress. The chemical valence state of Ti, Pd and Cu elements was further characterized by high-resolution XPS analysis. As shown in **Fig. 3b**, the high-resolution XPS spectrum of element Ti 2p displays doublet peaks located at 458.21 eV and 463.88 eV corresponding to the binding energies of Ti 2p 5/2 and Ti 2p 3/2, respectively, which are typical characteristics of Ti^{4+} [32]. **Fig. 3c** shows two small peaks centered at about 335.13 eV and 346.62 eV are in agreement with the binding energies of Pd 3d 5/2 and Pd 3d 3/2 of zero-valent Pd [33]. The relative weaker intensity of Pd 3d peaks mainly arise from the coating of Cu_2O shell on the surface of Pd as well as the limited detection depth of XPS. In the high-resolution XPS



Scheme 1. Schematic illustration for the preparation of ternary Z-scheme $\text{TiO}_2\text{-Pd-Cu}_2\text{O}$ hybrids.

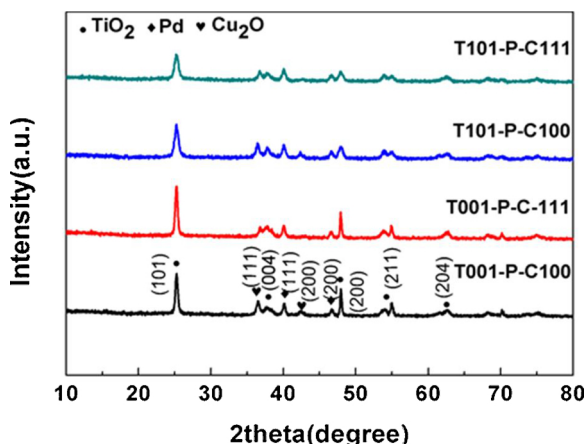


Fig. 1. XRD patterns of T001-P-C100, T001-P-C111, T101-P-C100 and T101-P-C111.

spectrum of Cu 2p (Fig. 3d), it can be recognized that two dominant peaks at 932.59 eV and 952.39 eV are assigned to Cu 2p 3/2 and Cu 2p 1/2 of that Cu (I) [34], while trace amount of Cu (II) was also detected and shown as two satellite peaks at 943.54 eV (Cu 2p 3/2) and 962.01 eV (Cu 2p 1/2), which are typical features for Cu_2O synthesized in solution-phase [35]. From these results, it can be concluded that the ternary $\text{TiO}_2\text{-Pd-Cu}_2\text{O}$ photocatalysts had been successfully prepared.

3.2. Charge kinetics and photocatalytic performance analysis

As the generation and transportation of photogenerated charges will influence the final photocatalytic performance, the charge kinetics of TiO_2 or Cu_2O based photocatalysts were investigated before conducting the photocatalytic degradation experiment.

The light absorption abilities of as-prepared samples, including T001, T101, C100, C111, T001-P-C100, T001-P-C111, T101-P-C100 and T101-P-C111, were revealed by UV-vis diffuse reflectance spectra. As shown in Fig. 4a, the DRS spectra of four $\text{TiO}_2\text{-Pd-Cu}_2\text{O}$ hybrids exhibit two main light absorption regions with absorption edges at

about 380 nm and 530 nm, corresponding to the inherent absorption of TiO_2 and Cu_2O . On one hand, compared two groups of TiO_2 based hybrids T101-P-C100 and T101-P-C111 with T001-P-C100 and T001-P-C111, it can be found that T101 based ternary hybrids display higher light harvesting capacities than those of T001 based hybrids, which is in accordance with the inherent light absorption abilities between T101 and T001 (Fig. 4b). On the other hand, two C100 based hybrids (T001-P-C100 and T101-P-C100) exhibit a similar light absorption profile in the visible region (400–500 nm) of DRS spectra, which is consistent with the inherent light absorption of C100. Similar phenomenon can also be observed from two C111 based hybrids (T001-P-C111 and T101-P-C111). Based on these results, it can be deduced that the light absorption properties of various facet based semiconductors (T001, T101, C100 and C111) were preserved in the corresponding ternary $\text{TiO}_2\text{-Pd-Cu}_2\text{O}$ hybrids. Furthermore, in comparison with single TiO_2 or Cu_2O , four $\text{TiO}_2\text{-Pd-Cu}_2\text{O}$ hybrids exhibit stronger light absorption in the region of 500–800 nm, which can be ascribed to the interband transitions of bound electrons in Pd [36,37]. The slight light harvesting abilities discrepancy between T001 and T101 (C100 and C111) would not affect the charge generation on $\text{TiO}_2\text{-Pd-Cu}_2\text{O}$ hybrids, and the efficiency of charge transfer can be reflected by the photocurrent response and the photoluminescence (PL) spectra results.

From Fig. 5a, it can be seen that the direct photocurrent responses for four $\text{TiO}_2\text{-Pd-Cu}_2\text{O}$ hybrids are in order of T101-P-C111 < T001-P-C111 < T101-P-C100 < T001-P-C100. Among them, T001-P-C100 exhibits improved photocurrent densities as compared with T001-P-C111 owing to the enhanced photogenerated holes transfer from C100 to Pd. Moreover, T001-P-C100 displays the highest photocurrent densities among the serial samples (Figure S4a, b), including T001, T001-P, C100 and P-C100, indicating the charge carriers separation efficiency was enhanced in this ternary hybrids system. Similar phenomenon was also observed between T101-P-C100 and T101-P-C111, the former exhibits higher photocurrent density than the later can also ascribe to the improved holes transfer ability from C100 to Pd. More importantly, as compared with T101-P-C100, the photocurrent density of T001-P-C100 is even enhanced, although the light absorption ability of T001-P-C100 is slightly weaker than that of T101-P-C100, which demonstrated the charges separation between TiO_2 and Pd instead of light absorption abilities play a more important role on the photocurrent density, and

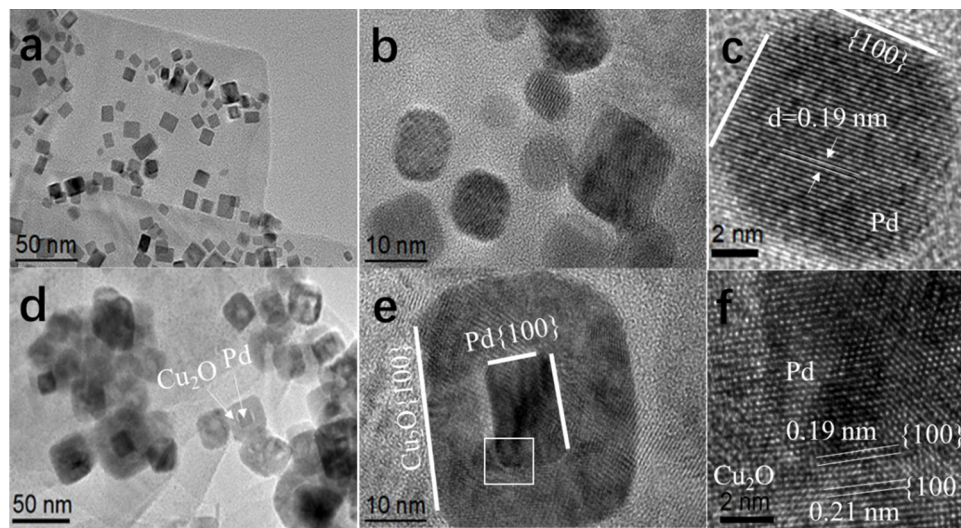


Fig. 2. (a, b) TEM and (c) HRTEM images of the T001-P precursor, (d, e) TEM and (f) HRTEM images of T001-P-C100 hybrid structure.

the electrons transfer from T001 to Pd was more efficient than that from T101 to Pd. The charge carriers separation performance was further investigated through collecting photoluminescence (PL) emission spectra at the excitation wavelength of 315 nm and 473 nm. As shown in Fig. 5b and c, the PL spectra of four TiO_2 -Pd-Cu₂O hybrids exhibit similar tendency with the aforementioned photocurrent results, with the weakest PL intensity observed for T001-P-C100, indicating its greatest inhibition of photogenerated electron-hole recombination process, while the strongest PL intensity was observed for T101-P-C111, which was attributed to its highest electron-hole recombination efficiency. Moreover, in comparison of the PL spectra of two groups TiO_2 based photocatalysts T001-P-C100 and T001-P-C111 with T101-P-C100 and T101-P-C111, it can be found that T001-P-C100 and T101-P-C100 exhibited relative weaker PL intensities in each group (Figure S5a, b), which further confirmed the holes transfer from C100 to Pd more

efficient than that from C111 to Pd. On the other hand, T001 was proved to possess better electrons giving abilities than T101, through horizontal comparing two groups of Cu₂O based photocatalysts C100-P-T001 and C100-P-T101 with C111-P-T001 and C111-P-T101 (Figure S5c, d).

To gain deeper insight into the influence of facet effects on charge transfer behaviors at the ternary TiO_2 -Pd-Cu₂O hybrids, the EIS Nyquist plots were measured. As shown in Fig. 5d, T001-P-C100 exhibits the smallest arc radius compared with other three TiO_2 -P-Cu₂O hybrids, indicating the lowest charge transfer resistance at the ternary T001-P-C100 hybrid interfaces, which can be ascribed to the suitable contact facets between TiO_2 , Cu₂O and Pd. In addition, the charge separation behaviors were further investigated by transient open-circuit voltage decay (OCVD) measurement [38], and the open circuit voltage (V_{oc}) decay dynamic can be estimated according to the following equation:

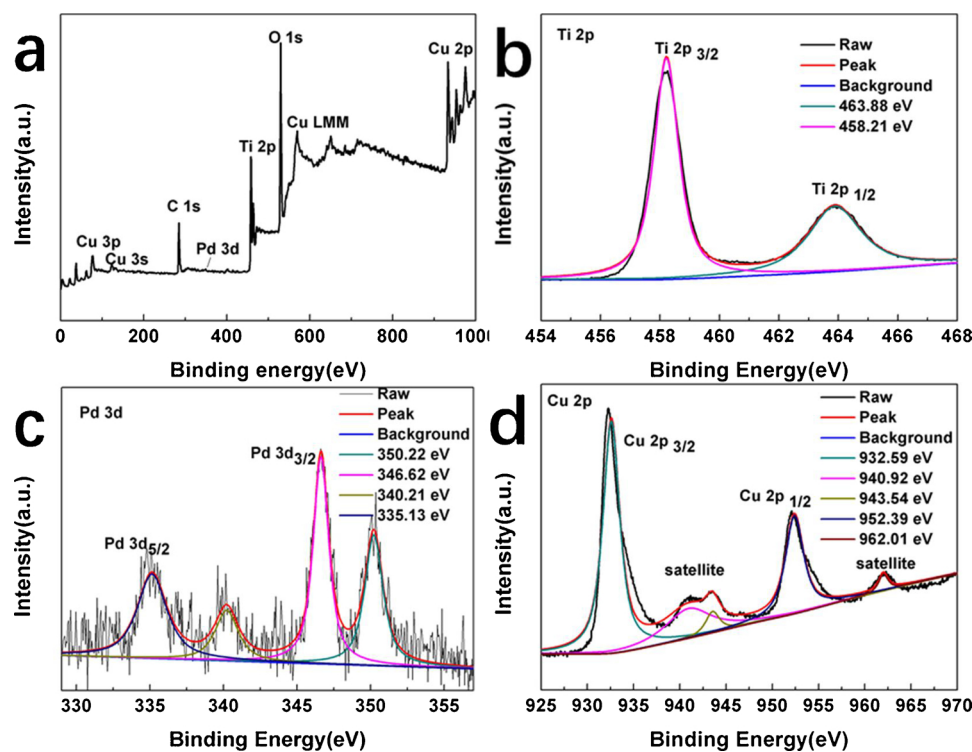


Fig. 3. XPS spectra of T001-P-C100: (a) survey spectrum, (b) Ti 2p, (c) Pd 3d and (d) Cu 2p high-resolution spectra.

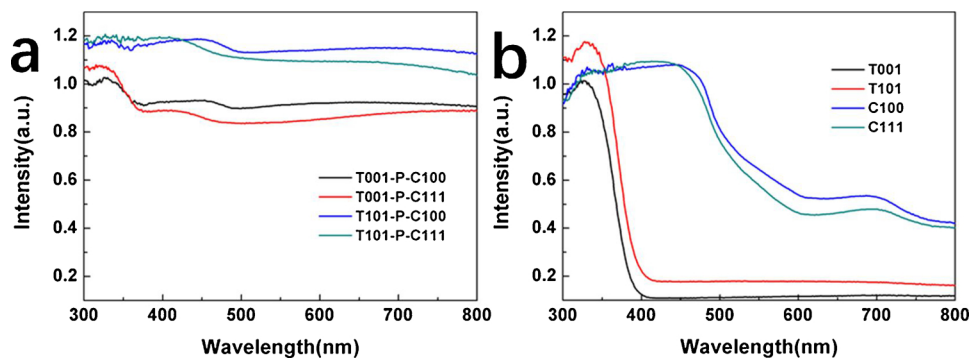


Fig. 4. UV – vis absorption spectra of (a) T001-P-C100, T001-P-C111, T101-P-C100 and T101-P-C111, (b) T001, T101, C100 and C111.

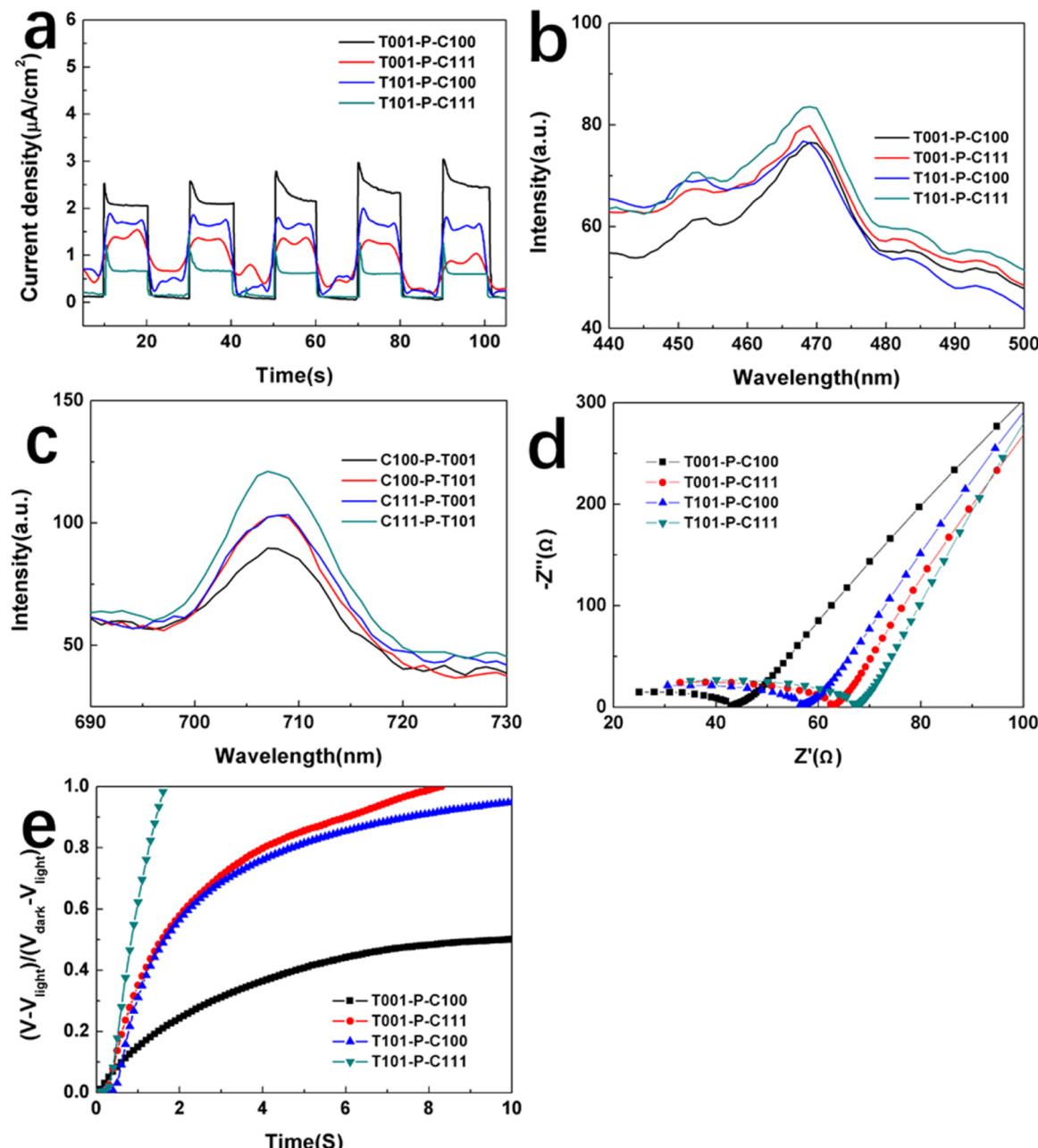


Fig. 5. (a) photocurrent response of T001-P-C100, T001-P-C111, T101-P-C100 and T101-P-C111, (b) PL spectra of TiO₂ based hybrids excited at 315 nm, (c) PL spectra of Cu₂O based catalysts excited at 473 nm, (d) EIS Nyquist plots and (e) normalized open-circuit potential decay curves of T001-P-C100, T001-P-C111, T101-P-C100 and T101-P-C111.

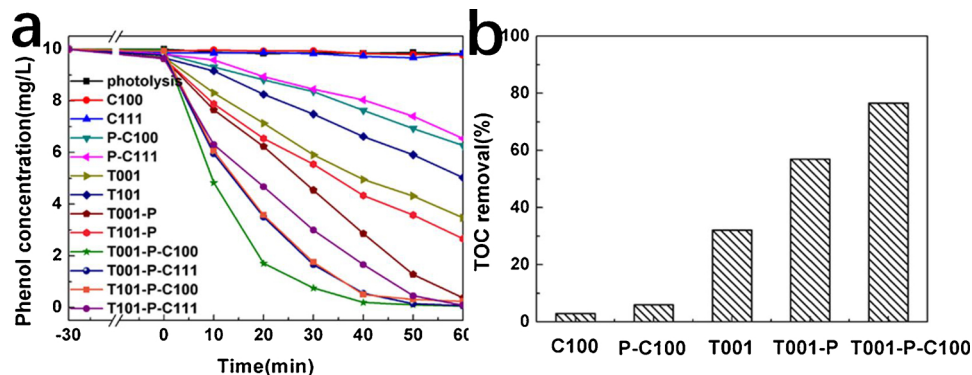


Fig. 6. (a) Phenol concentration versus time plots and (b) TOC removal of phenol during the photocatalytic process on different photocatalysts under simulated solar light irradiation ($\lambda = 320\text{--}780\text{ nm}$).

$$\frac{V - V_{\text{light}}}{V_{\text{dark}} - V_{\text{light}}} = 1 - e^{-kt}$$

Where k is the pseudo-first-order kinetic constant of recombination rate [39], V , V_{light} and V_{dark} correspond to V_{oc} at any time, under light irradiation and in the dark, respectively, and the results were illustrated in Fig. 5e. It can be seen that T001-P-C100 exhibits slowest decay kinetic, with a kinetic constant about 0.304 s^{-1} , followed by T101-P-C100 (0.407 s^{-1}) and T001-P-C111 (0.411 s^{-1}), while T101-P-C111 shows the highest decay kinetic (0.613 s^{-1}), which is accordance with the aforementioned demonstration and further confirmed the charge carriers recombination in T001-P-C100 is significantly suppressed.

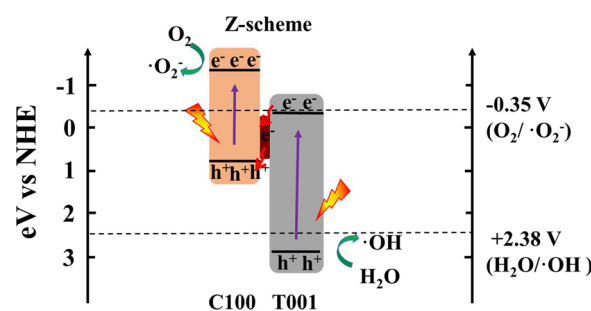
To evaluate the photocatalytic activity of as-prepared samples, phenol degradation was measured under simulated solar light irradiation ($\lambda = 320\text{--}780\text{ nm}$). From Fig. 6a, it can be observed that the concentration of phenol exhibits nearly no change without the addition of any photocatalysts, indicating it was stable under solar light irradiation. It is obvious that phenol degraded faster in the presence of four TiO₂-Pd-Cu₂O hybrids than in the presence of other TiO₂ and Cu₂O based photocatalysts, including T001, T001-P, T101, T101-P, C100, P-C100, C111 and P-C111, which can be ascribed to the enhanced charge carriers separation abilities and preserved high redox capacities in the ternary photocatalysts. Moreover, T001-P-C100 displayed the optimal photocatalytic performance for the degradation of phenol, with a kinetic rate constant of 0.0879 min^{-1} , which is higher than those of T001-P-C111 (0.0704 min^{-1}), T101-P-C100 (0.0721 min^{-1}) and T101-P-C111 (0.0426 min^{-1}) counterparts. The optimal photocatalytic performance of T001-P-C100 can be attributed to its suitable contact facets and energy band structure at the interface, which led to the superior interfacial charge carriers separation. This result was agreement with the aforementioned results of photocurrent density and photoluminescence tests. Meanwhile, T001-P-C100 was chosen as a typical example to further explore the mineralization capacity of ternary TiO₂-Pd-Cu₂O hybrids towards phenol, the total organic carbon (TOC) removal was measured and the results were displayed in Fig. 6b. It can be observed that the mineralization efficiency is evaluated to be about 76.5% for T001-P-C100 within 60 min reaction of phenol degradation, which was higher than those of single component, such as T001 (32.1%) and C100 (2.9%), because they suffered from either limit redox ability or poor charges separation capacity. Moreover, it was even higher than the sum of T001-P (57.0%) and P-C100 (5.9%), which can be ascribed to the synergistic effect between T001 and C100, leading to more holes on T001 with high oxidation capacity and more electrons on C100 with high reduction ability preserved in the ternary T001-P-C100 photocatalyst and finally degraded phenol into CO₂ and H₂O.

3.3. Photocatalytic mechanism analysis

To demonstrate the envisioned charge carriers transfer mechanism

of ternary TiO₂-Pd-Cu₂O hybrids, an ESR technique was employed to detect the transient radical intermediates with DMPO as a spin trap in the photocatalytic reaction system of T001, C100 and T001-P-C100 under simulated solar irradiation. According to the energy band alignments in Scheme 2, the energy levels of electrons on the conduction band of C100 are negative enough to reduce O₂ into ·O₂[−] radical ($E^{\circ}(O_2/O_2^-) = -0.35\text{ V vs NHE}$) [40]. As depicted in Fig. 7a, the signal of DMPO-O₂[−] adduct, six characteristic peaks with the standard ratio of intensities 1:1:1:1:1:1 [41], can be detected in the presence of C100 and its intensity is weaker than that of T001-P-C100, which indicated more electrons on C100 were preserved in the ternary T001-P-C100 photocatalyst. Moreover, no obvious characteristic peaks of the DMPO-·O₂[−] adduct was observed in the case of T001, indicating that little ·O₂[−] was produced in this system, owing to its relative positive conduction band position and high charge carriers recombination rate. Correspondingly, the energy levels of holes on the valence band of T001 are sufficiently positive to generate ·OH radical ($E^{\circ}(OH^-/OH) = 2.38\text{ V vs NHE}$) [40], while the holes on the valence band of C100 cannot achieve this goal due to its weak oxidation capacity. From the ·OH test results in Fig. 7b, it can be seen that the signal of the DMPO-OH adduct with four peaks with spectral line intensities 1:2:2:1 [42] was detected in both T001 and T001-P-C100, while no characteristic peak of DMPO-OH adduct was observed in the presence of C100. Furthermore, the stronger signal intensity observed in T001-P-C100 than that of in T001 can also ascribed to the efficient charge carrier transfer in T001-P-C100, which leaving more holes on the valence band of T001 in the ternary system than in single T001 photocatalyst. Based on above ESR results, it can be deduced that both electrons on the conduction band of C100 and holes on the valance band of T001 with high redox capacity were preserved during the photocatalytic process, indicating there is a Z-scheme charge carrier transfer mechanism in the ternary T001-P-C100.

In order to further demonstrate the contact facet induced interfacial charge carrier separation discrepancy in the Z-scheme TiO₂-Pd-Cu₂O hybrids, herein, a series of density functional theory (DFT) calculations



Scheme 2. Proposed photocatalytic mechanisms of T001-P-C100 hybrid.

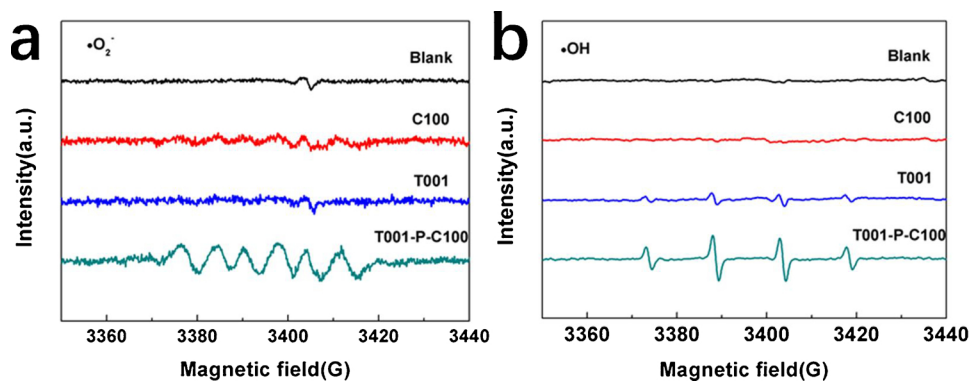
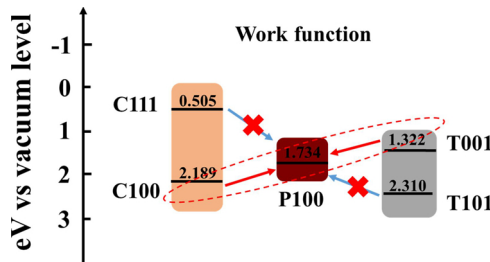


Fig. 7. ESR signals of (a) DMPO-O₂⁻ and DMPO-OH (b) adducts after 5 min irradiation in the presence of bare C100, bare T001 and T001-P-C100 photocatalysts ($\lambda = 320\text{--}780\text{ nm}$).



Scheme 3. Relative position of Fermi levels of C100, C111, P100, T001 and T101.

were performed and the relative position of work functions of different semiconductor facets (C100, C111, P100, T001 and T101) were illustrated in Scheme 3. It can be seen that the work function of C100, C111, P100, T001 and T101 were calculated to be 2.189 eV, 0.505 eV, 1.734 eV, 1.322 eV and 2.310 eV (Fig. 8a, b and Figure S6), respectively. Based on these results, T001 was inferred to be a good choice of

n-type semiconductor to establish the Schottky barrier with Pd in favor of the migration of electrons, because its work function is 0.412 eV lower than that of P100 [18]. Moreover, C100 with a 0.455 eV higher work function should also be a good candidate of p-type semiconductor to establish the Schottky barrier with Pd benefitting for the migration of holes. However, according to the potential lineup, the Schottky barrier cannot be formed at the T101-P and C111-P interfaces owing to the work function of T101 is 0.576 eV higher than P100, while C111 with a 1.229 eV lower work function than P100. These features disfavor both the migration of electrons from T101 to Pd and the transfer of holes from C111 to Pd, so that impaired the charge carrier separation at the T101-P and C111-P interfaces. Our simulation further investigated the potential lineup of ternary T001-P-C100 hybrid, and the relevant results were shown in Fig. 8c. It is clear that the work function of T001, P100 and C100 are in order of T001 < P100 < C100, which benefited the electron transportation from T001 via P100 to C100 at the T001-P-C100 interfaces through a Z-scheme mechanism. Furthermore, the differential charge density of T001-P-C100 hybrid was also calculated. The yellow and blue iso-surfaces in Fig. 8d represent the region of net

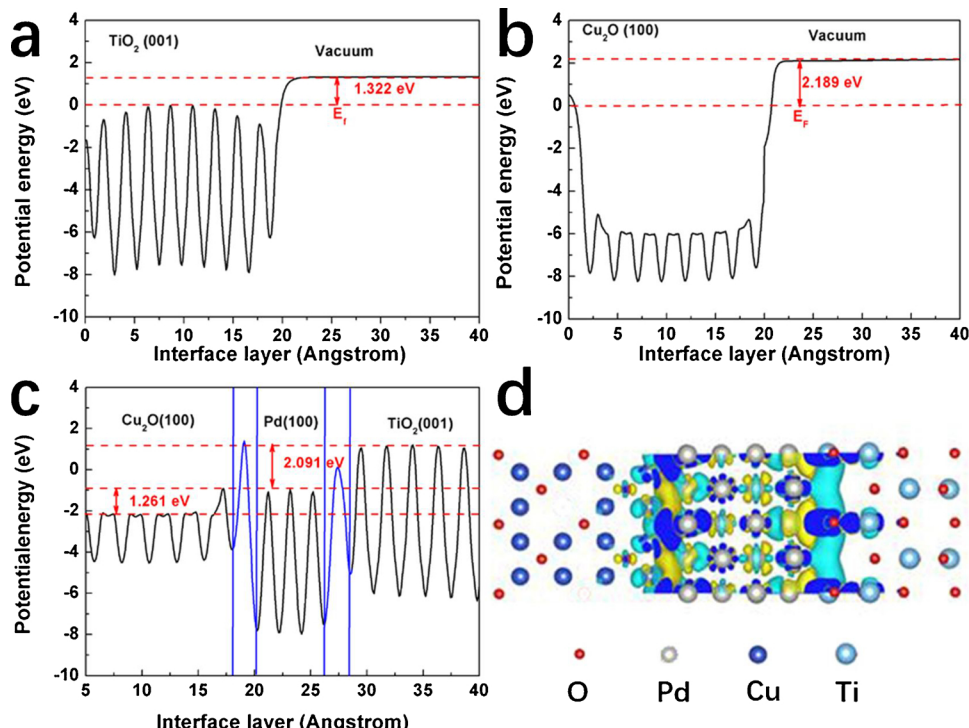


Fig. 8. Potential lineup of (a) T001, (b) C100 and (c) T001-P-C100 surface obtained from first-principles simulations. (d) Side-view differential charge density map of T001-P-C100.

electron accumulation and deficit, respectively. Apparently, the surface of Pd extracts electron and hole from adjacent T001 and C100, respectively. The DFT results qualitatively agree with the assumption that the interfaces formed among the T001, Pd and C100 lead to a more fluent charge carriers transfer and contribute to the higher photocatalytic performance than the T101-P-C111 case.

4. Conclusion

By controlling the different TiO_2 nanocrystal facets ($\{001\}$ facet or $\{101\}$ facet) as PS II and different Cu_2O nanocrystal facets ($\{100\}$ facet or $\{111\}$ facet) as PS I, four TiO_2 -Pd- Cu_2O hybrids were obtained to reveal the influence of facet effect on charge transfer across the interface of Z-scheme system. Both DFT calculation and experimental results confirmed that the Z-scheme T001-P-C100 hybrid possess superior charge separation ability and optimal photocatalytic activity than other three photocatalysts owing to the work functions at the interface of T001-P-C100 in order of $\text{TiO}_2\text{001} < \text{Pd} < \text{Cu}_2\text{O100}$, which leads to the formation of a favorable band alignment and further facilitated charge migration across the interface. An unfavorable band alignment was also used to explain the loss of photocatalytic activity upon constructing T101-P-C111 photocatalyst, which exhibited the inhibition of charge transfer and leading to inferior photocatalytic performance among the above four photocatalysts. This work casts new light on favorable Z-scheme interface design in consideration of facet-dependent band alignment, which is of importance to enhance the charge separation in the Z-scheme system and to further improve its efficiency.

Acknowledgements

This work was supported by National Natural Science Foundation of China (NO. 21590813), the Program of Introducing Talents of Discipline to Universities (B13012) and the programme for Chang Jiang Scholars and Innovative Research Team in University (IRT_13R05).

Appendix A. Supplementary data

Supplementary material related to this article can be found, in the online version, at doi:<https://doi.org/10.1016/j.apcatb.2018.10.066>.

References

- [1] P. Zhou, J.G. Yu, M. Jaroniec, All-solid-state Z-Scheme photocatalytic systems, *Adv Mater* 26 (2014) 4920–4935.
- [2] H.J. Li, W.G. Tu, Y. Zhou, Z.G. Zou, Z-scheme photocatalytic systems for promoting photocatalytic performance: recent progress and future challenges, *Adv. Sci.* 3 (2016) 1500389.
- [3] H. Tada, T. Mitsui, T. Kiyonaga, T. Akita, K. Tanaka, All-solid-state Z-Scheme in CdS -Au- TiO_2 three-component nanojunction system, *Nat. Mater.* 5 (2006) 782–786.
- [4] H.J. Yun, H. Lee, N.D. Kim, D.M. Lee, S. Yu, J. Yi, A combination of two visible-light responsive photocatalysts for achieving the Z-Scheme in the solid state, *ACS Nano* 5 (2011) 4084–4090.
- [5] A. Kudo, Y. Misaki, Heterogeneous photocatalyst materials for water splitting, *Chem. Soc. Rev.* 38 (2009) 253–278.
- [6] A. Iwase, Y.H. Ng, Y. Ishiguro, A. Kudo, R. Amal, Reduced graphene oxide as a solid-state electron mediator in Z-Scheme photocatalytic water splitting under visible light, *J. Am. Chem. Soc.* 133 (2011) 11054–11057.
- [7] M. Wang, Q.T. Han, L. Li, L.Q. Tang, H.J. Li, Y. Zhou, Z.G. Zou, Construction of an all-solid-state artificial Z-scheme system consisting of Bi_2WO_6 /Au/ CdS nanostructure for photocatalytic CO_2 reduction into renewable hydrocarbon fuel, *Nanotechnology* 28 (2017) 1–8.
- [8] R. Marschall, Semiconductor composites: strategies for enhancing charge carrier separation to improve photocatalytic activity, *Adv. Funct. Mater.* 24 (2014) 2421–2440.
- [9] K. Maeda, Z-scheme water splitting using two different semiconductor photocatalysts, *ACS Catal.* 3 (2013) 1486–1503.
- [10] K. Maeda, K. Domen, Photocatalytic water splitting: recent progress and future challenges, *J. Phys. Chem. Lett.* 1 (2010) 2655–2661.
- [11] H.F. Li, H.T. Yu, X. Quan, S. Chen, Y.B. Zhang, Uncovering the key role of the fermi level of the Electron mediator in a Z-Scheme photocatalyst by detecting the charge transfer process of WO_3 -metal-g₃_N₄ (Metal = Cu, Ag, Au), *ACS Appl. Mater. Interfaces* 8 (2016) 2111–2119.
- [12] F. Ye, H.F. Li, H.T. Yu, S. Chen, X. Quan, Constructing BiVO_4 -Au@ CdS photocatalyst with energetic charge-carrier separation capacity derived from facet induction and Z-scheme bridge for degradation of organic pollutants, *Appl. Catal. B* 227 (2018) 258–265.
- [13] S.C. Wu, C.S. Tan, M.H. Huang, Strong facet effects on interfacial charge transfer revealed through the examination of photocatalytic activities of various Cu_2O - ZnO heterostructures, *Adv. Funct. Mater.* 27 (2017) 1604635.
- [14] W.J. Yin, L.J. Bai, Y.Z. Zhu, S.X. Zhong, L.H. Zhao, Z.Q. Li, S. Bai, Embedding metal in the interface of a p-n heterojunction with a stack design for superior Z-Scheme photocatalytic hydrogen evolution, *ACS Appl. Mater. Interfaces* 8 (2016) 23133–23142.
- [15] J.Y. Ho, M.H. Huang, Synthesis of submicrometer-sized Cu_2O crystals with morphological evolution from cubic to hexapod structures and their comparative photocatalytic activity, *J. Phys. Chem. C* 113 (2009) 14159–14164.
- [16] S. Bai, J. Ge, L.L. Wang, M. Gong, M.S. Deng, Q. Kong, L. Song, J. Jiang, Q. Zhang, Y. Luo, Y.J. Xiong, A unique semiconductor-metal-Graphene stack design to harness charge flow for photocatalysis, *Adv. Mater.* 26 (2014) 5689–5695.
- [17] L.L. Wang, J. Ge, A.L. Wang, M.S. Deng, X.J. Wang, S. Bai, R. Li, J. Jiang, Q. Zhang, Y. Luo, Y.J. Xiong, Designing p-Type semiconductor-metal hybrid structures for improved photocatalysis, *Angew. Chem. Int. Ed. Engl.* 53 (2014) 5107–5111.
- [18] M.H. Cao, Z.Y. Tang, Q.P. Liu, Y. Xu, M. Chen, H.P. Lin, Y.Y. Li, E. Gross, Q. Zhang, The synergy between metal facet and oxide support facet for enhanced catalytic performance: the case of Pd-TiO₂, *Nano Lett.* 16 (2016) 5298–5302.
- [19] M. Li, Y. Chen, W. Li, X. Li, H. Tian, X. Wei, Z.H. Ren, G.R. Han, Ultrathin anatase TiO_2 nanosheets for high-performance photocatalytic hydrogen production, *Small* 13 (2017) 1604115.
- [20] M. Chen, J.Z. Ma, B. Zhang, G.Z. He, Y.B. Li, C.B. Zhang, H. He, Remarkable synergistic effect between $\{001\}$ facets and surface F ions promoting hole migration on anatase TiO_2 , *Appl. Catal. B* 207 (2017) 397–403.
- [21] Y.K. Lin, Y.J. Chiang, Y.J. Hsu, Metal- Cu_2O core-shell nanocrystals for gas sensing applications: effect of metal composition, *Sens. Actuators B-Chem.* 204 (2014) 190–196.
- [22] W.H. Ke, C.F. Hsia, Y.J. Chen, M.H. Huang, Synthesis of ultrasmall Cu_2O nanocubes and Octahedra with tunable sizes for facet-dependent optical property examination, *Small* 12 (2016) 3530–3534.
- [23] S. Rej, H.J. Wang, M.X. Huang, S.C. Hsu, C.S. Tan, F.C. Lin, J.S. Huang, M.H. Huang, Facet-dependent optical properties of Pd- Cu_2O core-shell nanocubes and octahedra, *Nanoscale* 7 (2015) 11135–11141.
- [24] G. Kresse, J. Furthmüller, Efficient iterative schemes for ab initio total-energy calculations using a plane-wave basis set, *Phys. Rev. B* 54 (1996) 11169–11186.
- [25] J.P. Perdew, K. Burke, M. Ernzerhof, Generalized gradient approximation made simple, *Phys. Rev. Lett.* 77 (1996) 3865–3868.
- [26] G. Kresse, D. Joubert, From ultrasoft pseudopotentials to the projector augmented-wave method, *Phys. Rev. B* 59 (1999) 1758–1775.
- [27] Z.A. Huang, Q. Sun, K.L. Lv, Z.H. Zhang, M. Li, B. Li, Effect of Contact Interface between TiO_2 and g-C₃N₄ on the Photoreactivity of g-C₃N₄/TiO₂ Photocatalyst: (001) vs (101) Facets of TiO₂, *Appl. Catal. B* 164 (2015) 420–427.
- [28] N. Liu, Y. Chang, Y.L. Feng, Y. Cheng, X.J. Sun, H. Jian, Y.Q. Feng, X. Li, H.Y. Zhang, {101}-{001} surface heterojunction-enhanced antibacterial activity of titanium dioxide nanocrystals under sunlight irradiation, *ACS Appl. Mater. Interfaces* 9 (2017) 5907–5915.
- [29] L. Ren, Y.Z. Li, J.T. Hou, J.L. Bai, M.Y. Mao, M. Zeng, X.J. Zhao, N. Li, The pivotal effect of the interaction between reactant and anatase TiO_2 nanosheets with exposed {001} facets on photocatalysis for the photocatalytic purification of VOCs, *Appl. Catal. B* 181 (2016) 625–634.
- [30] H.M. Wu, J.Z. Ma, Y.B. Li, C.B. Zhang, H. He, Photocatalytic oxidation of gaseous Ammonia over fluorinated TiO₂ with exposed (001) facets, *Appl. Catal. B* 152 (2014) 82–87.
- [31] Y.W. Wang, J.T. He, C.C. Liu, W.H. Chong, H.Y. Chen, Thermodynamics versus kinetics in Nanosynthesis, *Angew. Chem. Int. Ed. Engl.* 54 (2015) 2022–2051.
- [32] J. Chen, W.X. Song, H.S. Hou, Y. Zhang, M.J. Jing, X.N. Jia, X.B. Ji, Ti³⁺ self-doped dark rutile TiO₂ ultrafine nanorods with durable high-rate capability for lithium-ion batteries, *Adv. Funct. Mater.* 25 (2015) 6793–6801.
- [33] S. Ghosh, R.K. Sahu, C.R. Raj, Pt-Pd alloy nanoparticle-decorated carbon nanotubes: a durable and methanol tolerant oxygen reduction electrocatalyst, *Nanotechnology* 23 (2012) 385602.
- [34] C.E. Dube, B. Workie, S.P. Kounaves, A. Robbat, M.L. Aksu, G. Davies, Electrodeposition of metal alloy and mixed-oxide films using a single-precursor tetrานuclear copper-nickel complex, *J. Electrochem. Soc.* 142 (1995) 3357–3365.
- [35] Z.H. Ai, L.Z. Zhang, S.C. Lee, W.K. Ho, Interfacial hydrothermal synthesis of Cu@ Cu_2O core-shell microspheres with enhanced visible-light-Driven photocatalytic activity, *J. Phys. Chem. C* 113 (2009) 20896–20902.
- [36] S. Sarina, H.Y. Zhu, Q. Xiao, E. Jaatinen, J.F. Jia, Y.M. Huang, Z.F. Zheng, H.S. Wu, Viable photocatalysts under solar-spectrum irradiation: nonplasmonic metal nanoparticles, *Angew. Chem. Int. Ed. Engl.* 53 (2014) 2935–2940.
- [37] W.Y. Jiang, S. Bai, L.M. Wang, X.J. Wang, L. Yang, Y.R. Li, D. Liu, X.N. Wang, Z.Q. Li, J. Jiang, Y.J. Xiong, Integration of multiple plasmonic and co-catalyst nanostructures on TiO₂ nanosheets for visible-near-infrared photocatalytic hydrogen evolution, *Small* 12 (2016) 1640–1648.
- [38] Z.F. Jiang, W.M. Wan, H.M. Li, S.Q. Yuan, H.J. Zhao, P.K. Wong, A hierarchical Z-Scheme Alpha-Fe₂O₃/g-C₃N₄ hybrid for enhanced photocatalytic CO₂ reduction, *Adv. Mater.* 30 (2018) 1706108.
- [39] Z.F. Hu, Z.R. Shen, J.C. Yu, Covalent fixation of surface oxygen atoms on hematite photoanode for enhanced water oxidation, *Chem. Mater.* 28 (2016) 564–572.
- [40] D.A. Armstrong, R.E. Huie, W.H. Koppenol, S.V. Lymar, G. Merenyi, P. Neta, B. Rusic, D.M. Stanbury, S. Steenken, P. Wardman, Standard electrode potentials involving radicals in aqueous solution: inorganic radicals (IUPAC technical report), *Pure Appl. Chem.* 87 (2015) 1139–1150.
- [41] H.F. Li, X. Quan, S. Chen, H.T. Yu, Ferroelectric-enhanced Z-schematic electron transfer in BiVO₄-BiFeO₃-CuInS₂ for efficient photocatalytic pollutant degradation, *Appl. Catal. B* 209 (2017) 591–599.
- [42] Y.L. Yu, P. Zhang, Y.J. Kuang, Y.H. Ding, J.H. Yao, J.J. Xu, Y.A. Cao, Adjustment and control of energy levels for TiO₂-N/ZrO₂-N_x with enhanced visible light photocatalytic activity, *J. Phys. Chem. C* 118 (2014) 20982–20988.